SLAC-PUB-10448
June 2004

Radiative Characteristics of On-Chip Terahertz Undulatory Structures

Yasser A. Hussein, *Member, IEEE*, and James E. Spencer, *Member, IEEE*

***Abstract*—Work on compact, variable, efficient, and high brightness radiation sources is extended by calculating the radiated power and angular distributions for characteristic configurations and drive sources. On the assumption that the transport physics with Maxwell's Equations are valid but modified by the material properties, a number of analogs are suggested between free and bound electron sources of radiation. Characteristics of representative 1-to-n port examples are discussed in terms of a few basic shape parameters and the wavelength. Conditions for coherence and interference are discussed and demonstrated for the latter. Figures-of-merit are defined in terms of brightness, efficiencies or effective impedances such as the radiation coupling impedance Z_{rc}. Both time and frequency domain techniques are used and checked against other calculations and measurements where available. Finally, we discuss some further possibilities together with various impediments to realizing these kinds of devices such as the Terahertz (THz) modulation problem as well as nonlinear methods for their optimization. To our knowledge, there have been no implementations of such possibilities.**

***Index Term* —brightness, coherence, efficiencies, finite-difference time-domain (FDTD), high-frequency structure simulator (HFSS), interference, micro-undulators, sub-millimeter radiation, THz technologies.**

I. Introduction

PREVIOUSLY, we explored possibilities for producing narrow-band THz radiation using either free or bound electrons in micro-undulatory configurations [1] because integrated circuit technology appeared well matched to this region extending from about 300 GHz to 30 THz. This range [2]-[3] has largely been neglected until recently because it runs from the limit of WR-3 waveguide around 300 GHz up to CO_2 lasers where the laser regime becomes dominant.

The present work is a byproduct of an ongoing goal of making an electro-optic electron accelerator on a chip or AOC. While lasers provide sufficient power for such applications, their use generally implies effective cell sizes proportional to their wavelength, which poses a major complication. Thus, devices bridging the gap between lasers and conventional RF could prove very useful.

Manuscript received April 21, 2004. This work was supported by the U.S. Department of Energy under Contract *DE-ACO3-76SF00515*BS123456.

Y. A. Hussein is with the Stanford Linear Accelerator Center, Stanford University, Menlo Park, CA 94025 USA (phone: 650-926-8602; fax: 650-926-4365; e-mail: yasser@ slac.stanford.edu).

J. E. Spencer is with the Stanford Linear Accelerator Center, Stanford University, Menlo Park, CA 94025 USA (phone: 650-926-3385; fax: 650-926-4365; e-mail: jus@ slac.stanford.edu).

Because of their other potential uses [2], we decided to explore this THz region using wiggler or snake-like configurations such as shown in Fig. 1.

Of particular importance here was the fact that examples of such structures had been printed using gold on silicon wafers having different periods and wavelengths [4] with dimensions scaled to give the same low frequency impedances for the same number of periods N. Pulse currents greater than 1 A at 1 ns were obtained routinely without failures up to the largest N that were made of N=20. This was achieved by carefully conditioning the circuits with increasingly larger DC currents while monitoring the resistance to avoid runaway before backing off, cool down and then going to higher currents. We have yet to find a current limit due to lack of the needed sources that far exceed those typically available or compatible with probe stations.

This paper is organized as follows: Section II gives a general discussion, Section III provides nomenclature and FDTD code validation is given in Section IV. FDTD results are given in Section V and radiation calculations are presented in Section VI. Section VII defines another figure-of-merit. Conclusions and future research are given in Section VIII.

II. General Discussion

For idealized cases and for understanding more complex configurations with realistic physical properties, the most direct approach is to determine the Poynting vector based on calculating the acceleration fields in the far field and from it the angular distribution. The most useful formulation here is in terms of the source current density:

$$\frac{dP}{d\Omega} = \frac{1}{4\pi c^3}\left\{ \boldsymbol{n} \times \int \frac{\partial \boldsymbol{J}(\boldsymbol{r}',t_r)}{\partial t} d\boldsymbol{r}' \right\}^2 \qquad (1)$$

where t_r is the retarded time between source and detector, $\boldsymbol{J}$ is the current density, P is the power, and c is the light velocity in free space. For $\beta \equiv \boldsymbol{v}/c << 1$, the above relation reduces to the Larmor relations:

$$\frac{dP}{d\Omega} = \frac{e^2}{4\pi c^3}\left\{ \frac{d\boldsymbol{v}(t)}{dt} \right\}^2 \sin^2\theta \quad \text{and} \quad P = \frac{2}{3}\frac{e^2}{c^3}\left\{ \frac{d\boldsymbol{v}(t)}{dt} \right\}^2 \qquad (2)$$

where θ is the angle between the observation direction $\boldsymbol{n}$ and the direction of acceleration at emission time t. A straightforward application of Eq. (1) was given in Eq. (1) of Ref. [1] where we noted that a beam of free electrons in an undulator that provides a sinusoidal magnetic field with

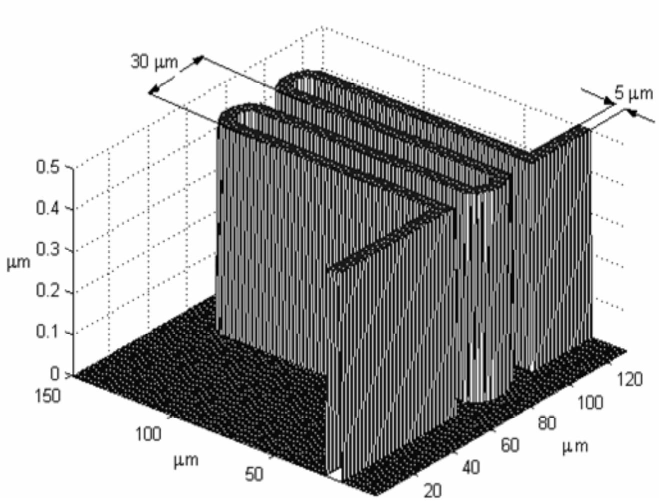

Fig. 1. Planar lattice (not to scale) for 1.5 periods of a 2-D wiggler (undulator) with the vertical representing a perfect conductor of 0.5 µm thickness and "0" a dielectric substrate (Duriod: relative permittivity of 2.2).

wavelength λ_U would produce harmonics q of the device wavelength:

$$\lambda \sim \frac{\lambda_U}{2q\gamma^2} \tag{3}$$

where the electron energy γ is in units of rest mass mc^2. The energy is squared as a result of transforming to the electron rest frame where a pure dipole oscillation occurs (q =1). This is under the condition that the electric field doesn't accelerate the electron sufficiently to cause figure-eight motion, i.e. that the motion remains highly non-relativistic. The distribution is then transformed back into the laboratory frame where it is contracted into the forward direction within an opening angle $\delta\theta \sim 1/\gamma$. Under these circumstances, the amplitude of the Poynting vector $|\boldsymbol{S}|$ equals to $n_\gamma \hbar\omega c$, where n_γ is the photon number density. To increase photon frequency, one can increase γ or reduce λ_U or the effective mass m*. For low-energy, conduction-band electrons, $\gamma \sim 1$ so that a wiggle period of $\lambda_U = 60$µm, achievable with standard IC techniques, might be expected to give 30 µm, 10 THz radiation.

We explore the validity of these ideas and ways to implement such devices noting that interference occurs in this free electron case through slippage of the electron by one radiation wavelength λ over a traversal of one wiggler wavelength λ_U, while coherence is expected when $\lambda \gg l_e$, the inter-electron spacing. To account for the latter, we can define an effective charge e^*, which can be quite large in units of e. In this free electron case, the radiation is electromagnetic in origin whereas in some of the bound examples we discuss it is more properly called electromechanical.

III. Some Nomenclature

In a typical, 2-port, lossy, microwave structure, the power dissipated (normalized to the input power) can be estimated on the assumption that the S-matrix is complex and orthogonal as:

$$P_l = 1 - |S_{11}|^2 - |S_{21}|^2 \geq 0. \tag{4}$$

The power dissipated can be due to radiation, conductor or substrate loss. For instance, for a standard radiating structure with no output port (S_{21}=0), the dissipated power is dependent on S_{11} only. In this case, small values of S_{11} indicate high loss. Further, if we assume no conductor or substrate loss, the radiated power must go inversely as $|S_{11}|^2$. If one defines the radiation efficiency as:

$$\eta = \frac{P_r}{P_l} \tag{5}$$

then this radiating structure has 100% radiation efficiency since all the power dissipated is due to radiation. If a second port exists, the dissipated power must depend on the transmission coefficient as well (S_{21}), with higher transmission indicating lower losses. Clearly, if part of the dissipated power is due to substrate and/or conductor loss, the radiation efficiency in this case, based on (5), will be less than 100%. An example of this is the half-period wiggler where a portion of the loss is dissipated in the substrate (the substrate is assumed to be lossy with a small loss tangent value). Another definition for the radiation efficiency can be given as:

$$\eta = \frac{P_r}{P_t} \tag{6}$$

where P_t is the total power applied to the structure, so the efficiency is the percentage of power lost into radiation compared to the total power applied to the structure-ideally the so-called wall-plug power. Before proceeding to any calculations we first discuss the codes and some tests and comparisons that were done.

IV. FDTD Code Validation

Finite Difference Time Domain (FDTD) is a powerful and flexible technique that is expected to play a central role in development and simulation of sub-millimeter wave devices. It was chosen here because it is very efficient and its implementation is straightforward. It is ideal for our problem which is non-linear, may include anisotropies, and where high pulsed currents are important.

Before attempting any simulations, the developed FDTD code required validation. The results are compared to those

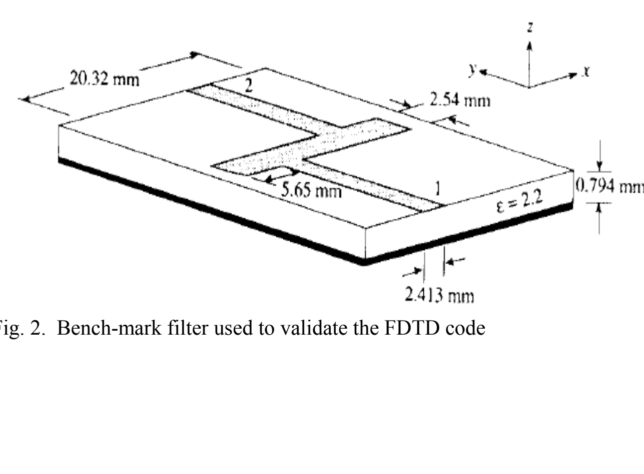

Fig. 2. Bench-mark filter used to validate the FDTD code

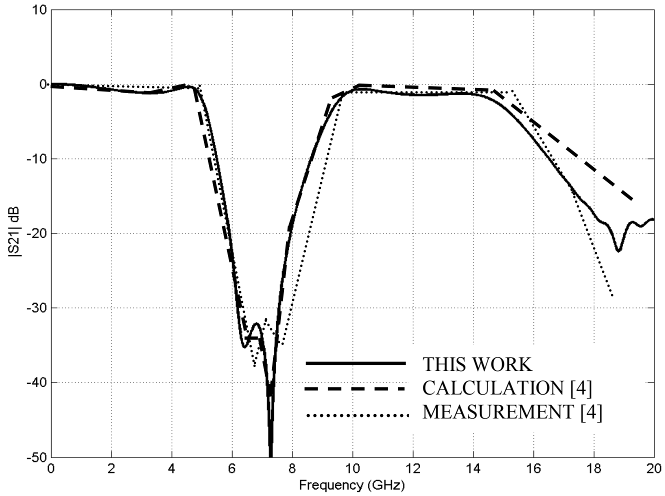

Fig. 3. Insertion loss comparison curves for the low-pass filter.

presented in [5]. The low-pass filter that was used is shown in Fig. 2. Comparison results for the insertion loss (S_{21}) and return loss (S_{11}) are shown in Figs. 3 and 4. One observes good agreement with measured and calculated data except for the highest frequency which is somewhat shifted. Experimentation with planar circuit techniques leads one to conclude that this shift is caused mainly by the slight misplacement of the ports inherent in the choice of the spatial steps [5].

Good agreement between the results obtained using FDTD methods [6] and HFSS [7] were observed in all cases that were compared. Figures 5 and 6 give sample comparison curves between the FDTD codes developed in this paper and HFSS for the return loss and radiation efficiency. These results are obtained from simulating the structures shown in Fig. 18, when d=0 and Fig. 13, when T=0. It is important to note that the S-parameters were calculated using both HFSS and the FDTD codes at the same reference plane. More discussion, results and analysis of these and other configurations will be discussed in later sections.

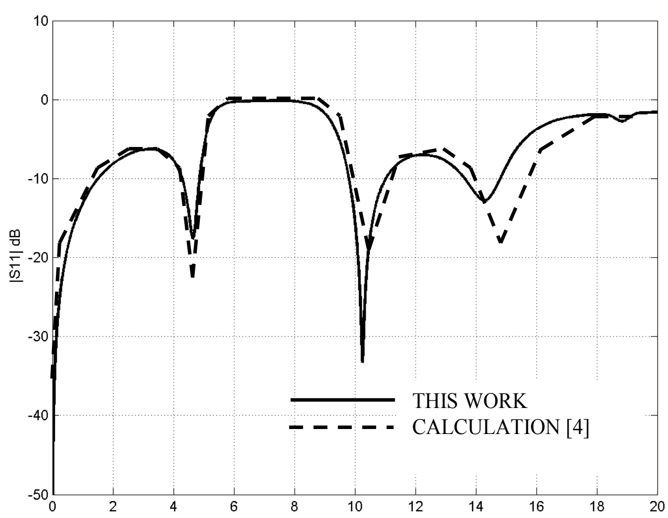

Fig. 4. Return loss comparison curves for the low-pass filter

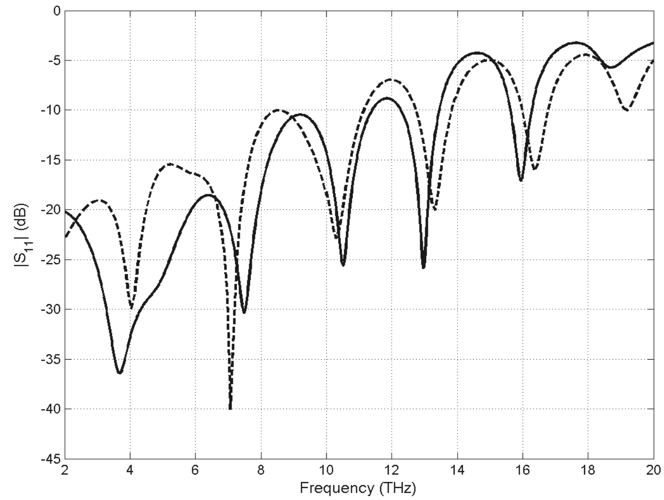

Fig. 5. Return loss, FDTD (solid) and HFSS(dashed) for the structure shown in Fig. 18.

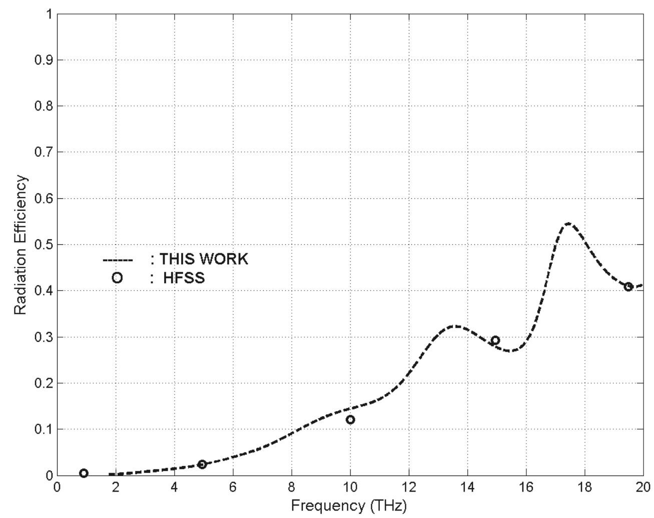

Fig. 6. Radiation efficiency comparison curves for the structure shown in Fig. 13.

V. Some Examples and Results

FDTD simulations were carried out for such structures as shown in Fig. 1, where the half-period circuit length L is 231.4 μm for λ_U=30 μm. This gives a fundamental resonant frequency f_0 of 0.437 THz. This is not f_U for a free electron from Eq. (3). The return and insertion losses for a half period are shown in Fig. 7, normalized to the frequency f_0. Figure 8 shows the corresponding results for 1.5 periods for comparison. None of these structures, in this form, are expected to be coherent but are expected to provide constructive interference under certain types of excitation.

Figure 7 shows that an electron wave passes through the structure with very small reflection at f_0 because it is matched and doesn't resolve the half loop well at this long wavelength, so there is virtually no reflection. Further, the broad reflections around 2, 4, 6, and 8 f_0 are due to harmonics of the reflection coming from the loop at ¼ of the wiggler period. As the frequency increases, the reflection coefficient increases and broadens consistent with the fact that higher frequencies resolve and sample the full loop better. From Ref. [1] we estimated a radiation rate of ~0.03 photons per electron per half loop, assuming neither interference nor coherence effects, with a diffuse pattern based on an angular spread of ~1/γ radians. We will return to this later, after calculating the radiation fields, where one can view the patterns in more detail as truncated dipole oscillations. While not optimal for brightness, it does imply out-of-plane radiation in contrast to the relativistic, free case. We also expect the reflected electrons to radiate photons with a different radiation pattern in a competitive way because γ ~1.

In Fig. 8, the broad reflections around 2, 4, 6, and 8 f_0 also exist for the 1.5 period case except that there are now loops at ~1/2, 3/2, 5/2 f_0 etc. Ideally, these sidebands on either side of the main radiation peaks multiply but become more muted with increasing number of periods N as inferred from Fig. 7. In the same way, one sees that the strong reflections increase with increasing periods in direct analogy with high reflector (HR) optical coatings. The dual character of the return and insertion loss parameters is clear in Fig's. 7 - 8. Generally, one might expect to see interference effects with such structures when using a sinusoidal drive source and proper tuning of the circuit parameters based on the modulation of the side bands with increasing frequency in this rather arbitrary case. For completeness, Fig. 9 shows the input impedance (real and imaginary) as a function of frequency. At deep resonance, the input impedances are purely real (50Ω). This corresponds to a matching load that has zero reflection and is close to what was observed with the integrated circuit examples that we studied e.g. for N=20, with different wavelengths, a resistance of ~72 Ω was observed. Under the assumption of ballistic transport, this implies a broad band radiation spectrum having the mean energy given by Eq. (3) of Ref. [1].

Figure 10 shows the radiation efficiency as a function of the normalized frequency for the half-period wiggler. One observes that the radiation efficiency increases with frequency. In addition, the radiation efficiency maxima track the minimum of S_{21}, which occur around 2, 4, 6, 8, and 10 f_0 as discussed above. It is noteworthy to underline that the resonant frequencies are estimated based on a constant relative permittivity. This explains the results in the previous figures, where the high resonant frequency values are overestimated because the effect of the increase of relative permittivity with frequency is not included. A simple estimate for the relative permittivity at 10 f_0 gives ~ 1.1 ϵ_r (f_0).

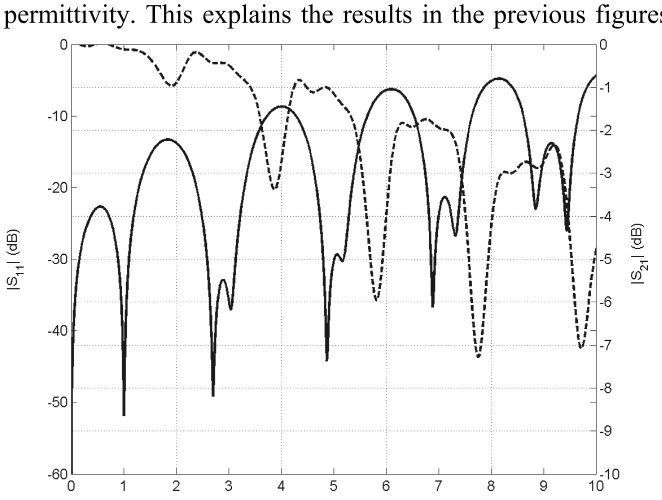

Fig. 7. Insertion (dashed) and return (solid) losses versus f / f_0 for the half-period case.

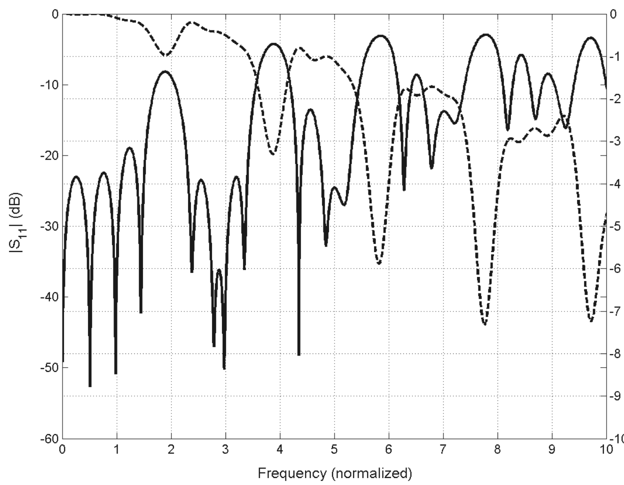

Fig. 8. Insertion (dashed) and return (solid) losses versus f / f_0 for the 1.5 period case.

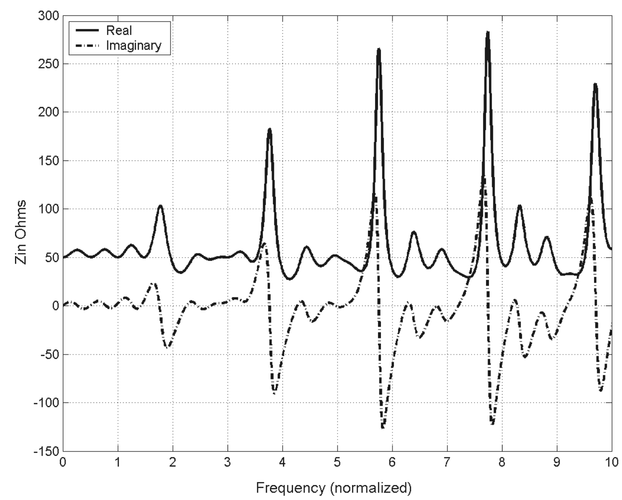

Fig. 9. Input impedance versus f / f_0 for the 1.5 period wiggler.

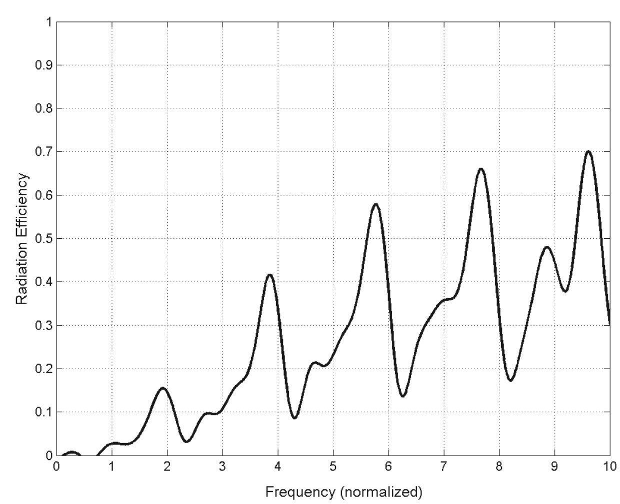

Fig. 10. Radiation efficiency from Eq. (6) versus f / f_0 for the 0.5 period wiggler

VI. Radiation Calculations

Detailed HFSS simulations were carried out to calculate the radiation patterns for several configurations. The half-period layout and radiation pattern for φ=90˚ (the YZ plane) is shown in detail in Fig. 11 for different frequencies, with the angle θ starting from the –y axis. One observes that higher frequencies have higher radiated power while S_{11} trends higher and S_{21} decreases with frequency. Because the value of S_{21} (close to unity) is higher than S_{11} (close to zero), the radiated power tracks S_{21} at the lower frequencies, which is the preferred alternative. This is where the most obvious dipole element becomes resonant corresponding to the long period loop extending from the input line to the output line. One can decompose this half period structure into a sequence of idealized zero-width, constant-current dipole antennas where the lowest frequencies are dominated by a simple $\sin^2\theta$ distribution from Eqs. (1) - (2) based on an oscillation along the y axis.

Further, at higher frequencies and still looking at the YZ plane, the 90˚ turns that were put in to avoid crosstalk between input and output ports as well as a well-defined loop, begin to be resolved. These explain why S_{11} increases and S_{21} decreases. They can be viewed as two dipoles at 90˚ to one another, which become dominant at the highest frequency in Fig. 11 producing the double-lobed distribution. As discussed above these show an expected angular spread of ~1/γ or about 1 radian.

For a simplified dipole antenna oriented along the y axis, the characteristic parameters are λ and ℓ where $\ell \approx L/2$ and the current density is $J_y(t) = (e\upsilon)\sin(\omega t)\delta(x)\delta(z)$. Averaged over one cycle, this gives an angular distribution:

$$\frac{dP}{d\Omega} = \frac{I^2}{2\pi c} \frac{\sin(\theta)^2 \cdot \sin(\frac{\pi l}{\lambda}\cos(\theta))^2}{\cos(\theta)^2} \quad (7)$$

Figure 12 shows the radiation pattern at φ =0 (the XZ plane) for different frequencies, with the angle θ starting from the –x axis. One observes again that the radiated power increases with frequency. Further, the radiation pattern, while similar to Fig. 11, is unsymmetrical. One can understand such features from the existence of more than one effective radiator and Eq. (7) for our primary radiator. Beginning at the lowest frequencies, e.g. f_0 where $\lambda \approx 4\ell$, we can take $\lambda \gg \ell$, which reduces Eq. (7) to:

$$\frac{dP}{d\Omega} = \frac{I^2}{2\pi c} (\frac{\pi l}{\lambda})^2 \sin(\theta)^2 \quad (8)$$

which peaks at θ=90˚ and increases as f^2 or ω^2, which is roughly consistent with the two lowest frequencies in Figs 11 - 12. Further, only one lobe exists in this regime but these conditions quickly saturate as does the symmetry with decreasing wavelength λ until, for › λ, one expects additional side lobes to begin to appear beginning at $\theta = \cos^{-1}(\lambda/\ell)$.

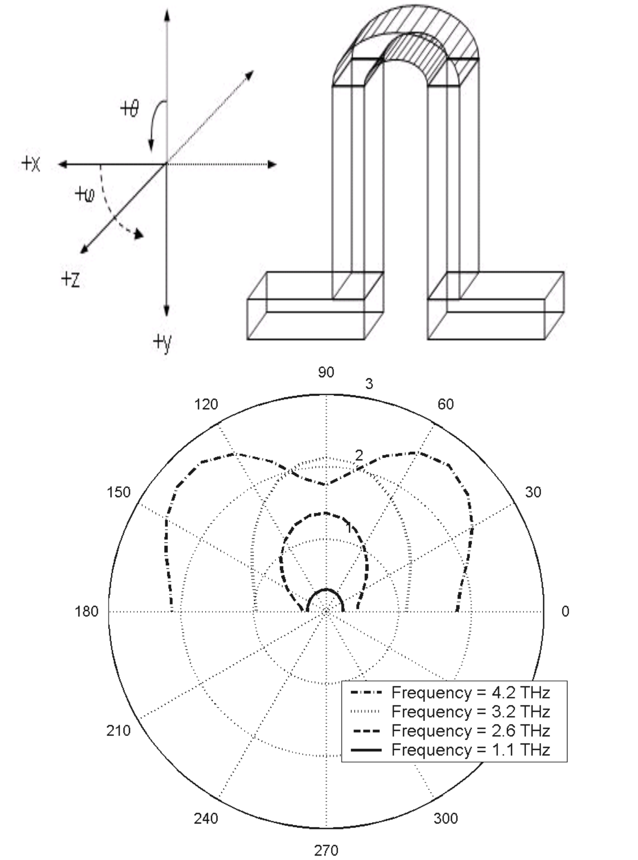

Fig. 11. Radiation pattern for the total electric field at φ = 90˚ for different frequencies.

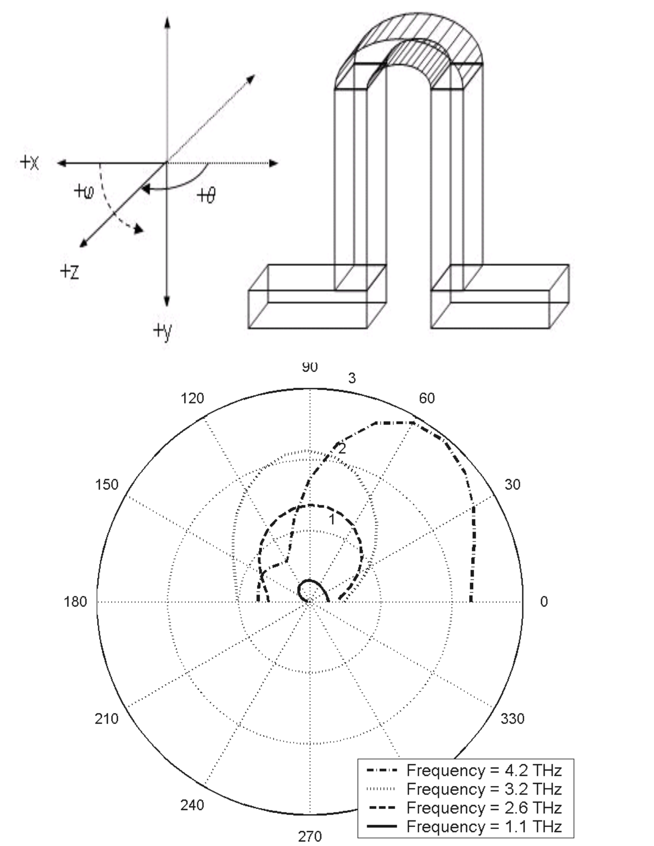

Fig. 12. Radiation pattern for the total electric field at φ = 0˚ for different frequencies.

A. Further One-Loop Calculations

To investigate further the characteristics of the half-period wiggler, the lengths of the two transmission lines (T) at either side of the wiggler are varied so that the half-circle is connected to the ports via transmission lines of length T. As a result, the first resonant frequency should occur at a higher/lower frequency, which can be checked by looking at the S-parameters curves, Figs. 7, 14 and 15. Further, one finds that the resonant frequencies for such planar circuits follow Eq. (9) when properly applied:

$$f_{l,m} = \frac{c}{\sqrt{\epsilon_{eff}}}\sqrt{\frac{l^2}{(2a)^2}+\frac{m^2}{(2b)^2}} \tag{9}$$

with $a = L =$ 2W+T+R and $b = \pi$R+ 2T. It is also worth noting that the purpose of reducing the length T is not only to have radiation at higher frequencies but also to achieve a more pure dipole-like radiation pattern at these frequencies.

HFSS simulations were carried out to calculate the radiative characteristics for Case 1 of Figs. 13-15 are shown in Fig. 16 (for φ=90°) and Fig. 17. In Fig. 16 at f = 4.0 THz, one sees that the radiation comes out predominately perpendicular to the surface and is more symmetric and dipole-like in contrast to the original example (Fig. 11) - especially at 4.2 THz, where the radiation pattern was more diffuse with worse directivity. At higher frequencies, the patterns become increasingly reticulated as discussed above in relation to Eq. 7. Also, one observes that tradeoffs exist between the radiation efficiency and directivity. This is most noticeable in the peak values of the radiated electric fields, which show that the efficiency of the original case is higher than for that shown in Fig. 13. However, this is not significant considering the better directivity and the improved possibilities for constructive interference when we add periods. It is worth noting that the legends of Fig. 16 are for much higher frequencies than those in Fig. 11. Finally, Fig. 17 shows the 3D radiation patterns at different frequencies, where one again observes that the radiation patterns become increasingly distorted at the higher frequencies.

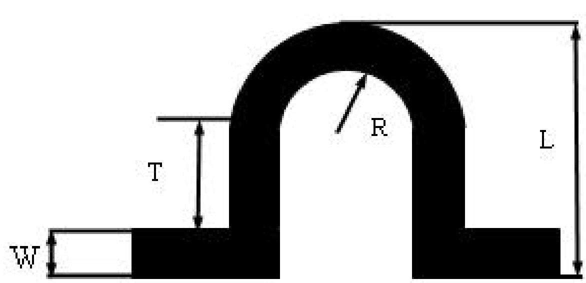

Fig. 13. Top-view of the 0.5 period case (not to scale). R = 4 μm, W = 2 μm, and T = 0, 2, and 3.2 μm.

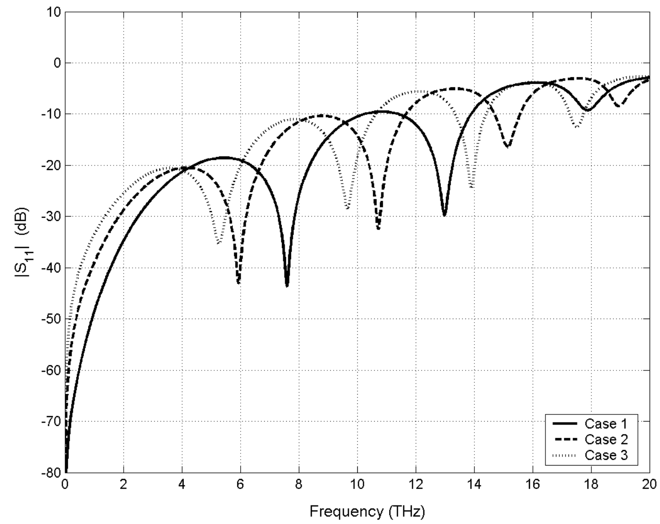

Fig. 14. Return loss versus frequency for the half-period case in Fig. (13). Case 1: T= 0 μm. Case 2: T= 2 μm. Case 3: T= 3.2 μm.

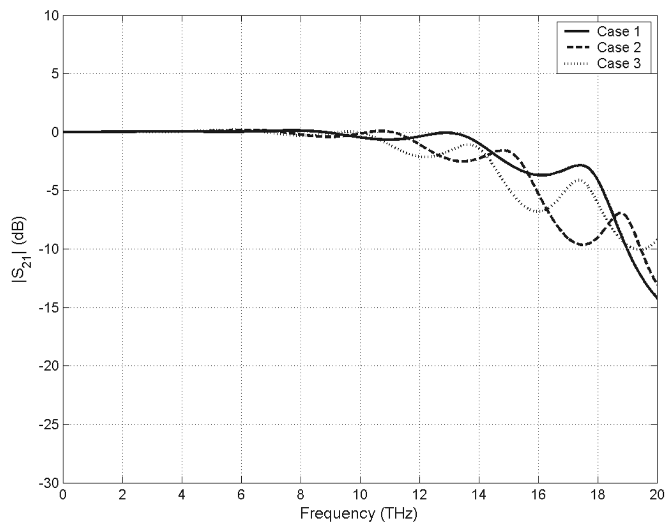

Fig. 15. Insertion loss for the half-period cases in Fig. (13) where Case 1: T= 0 μm, etc.

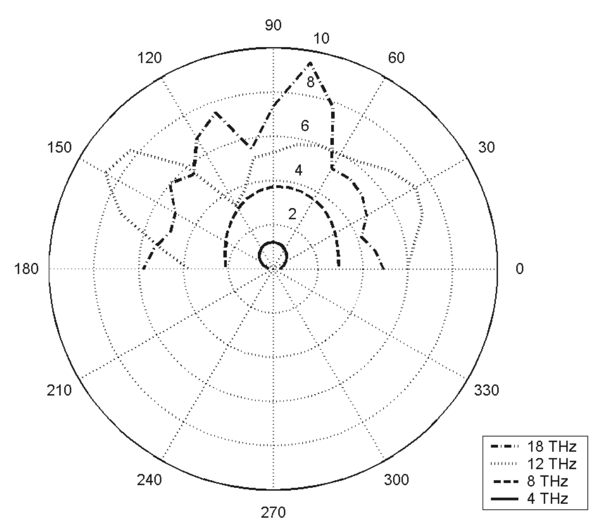

Fig. 16. Radiation pattern for the total electric field at φ=90° for different frequencies

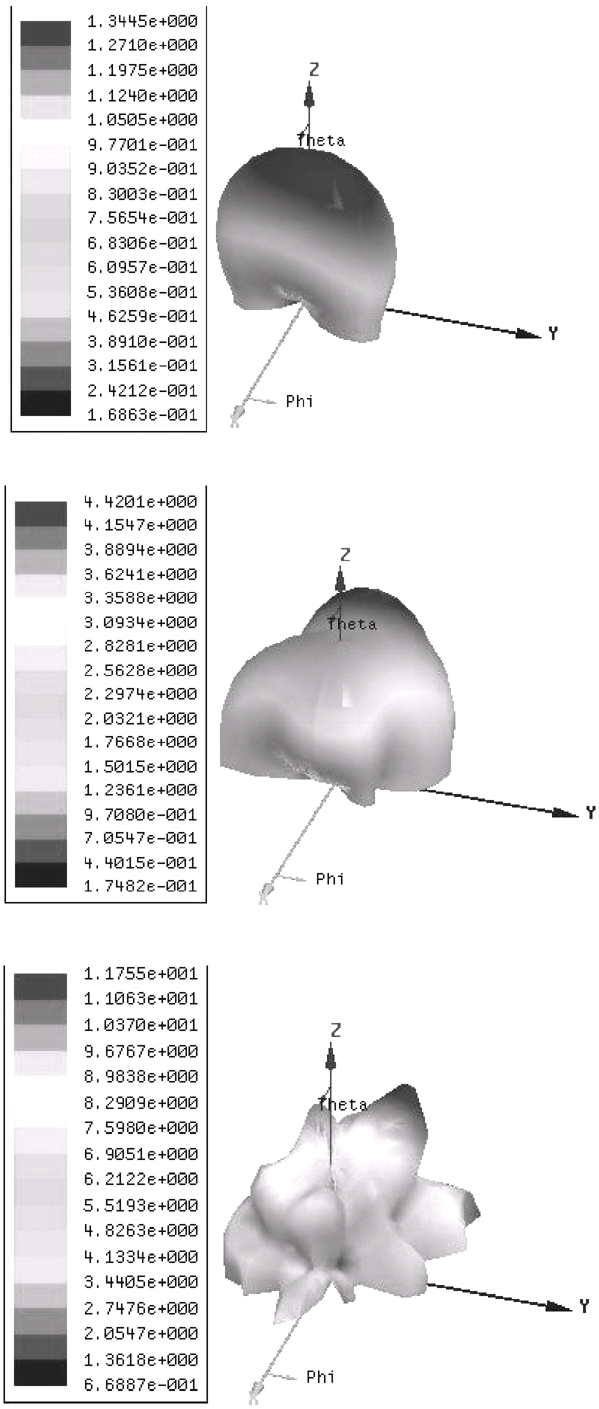

Fig. 17. 3-D radiation pattern (mV) at 4, 8, and 18 THz

B. Two-Loop, One-Period N=1, d=0 Examples

In this section, a second half circle is added to the first one on the same transmission line, with one facing up and the other down but with the tuning distance $d = 0$ in Fig. 18.

The return loss is shown in Fig. 5 of the code validation section for comparison to Case 1 in Fig. 13. One observes that a new resonant frequency is created at 3.8 THz, which corresponds to twice the wavelength of a single half-circle (7.9 THz). Good agreement between the results obtained by the FDTD code and HFSS was observed. As expected, the number of resonant frequencies is doubled over the same frequency range. Fig. 19 shows the radiation efficiency versus frequency for three different cases, where Case 3 rearranges the ports to eliminate the 90º turns used in all previous cases. The radiation efficiency is increased over the one-loop examples, e.g. Case 1, because there are two half-circles radiating instead of one but this is mediated by several competing effects. If there were no destructive or constructive interference then, at best, one expects only a doubling of the power.

Clearly, the situation is more complicated. First, because the one-loop case has different (higher) resonant frequencies, the power is superficially lower in Fig. 19. As a result, the background level follows a more obvious quadratic dependence on frequency. Still, comparing Cases 1 and 3, where there is less resonant structure than for Case 2, there is parabolic structure in both curves albeit most clear at the lower frequencies. Using these trends, shifting the curves to compare comparable resonances and averaging gives a crude power doubling between the one and two loop cases at intermediate frequencies. Similarly, comparing Cases 2 and 3 for the two, double-loop cases, we see nearly perfect interference doubling of the power at the lowest two, strong resonances but which gets successively worse with increasing frequency as the characteristic size of the radiator comes into match with the radiated wavelength.

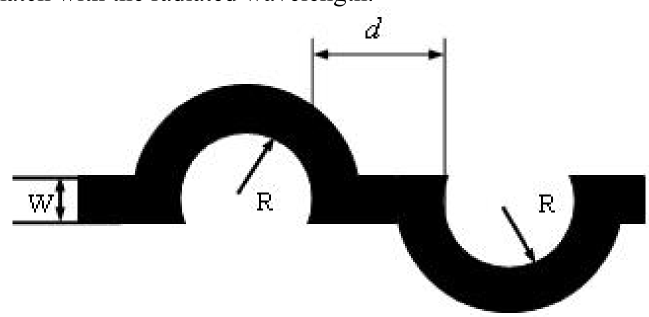

Fig. 18. Top-view of two half-circles (not to scale) separated by a distance d. R = 4 μm and W= 2 μm.

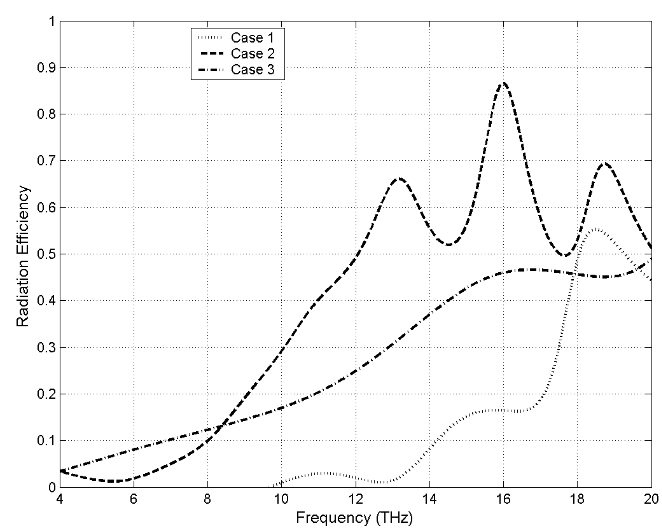

Fig. 19. Radiation efficiency curves for three cases (d=0). Case 1: single half-circle. Case 2: two half-circles. Case 3: two half-circles without 90º turns based on rearranging ports.

Figures 20-22 show the radiation patterns for some characteristic frequencies of Case 2. Noting that θ=90˚ is the preferred direction perpendicular to the circuit plane in both Figs. 20 and 21, it follows that the preferred frequency is at the 16 THz resonance, which is stronger and more directed than any of the previous examples.

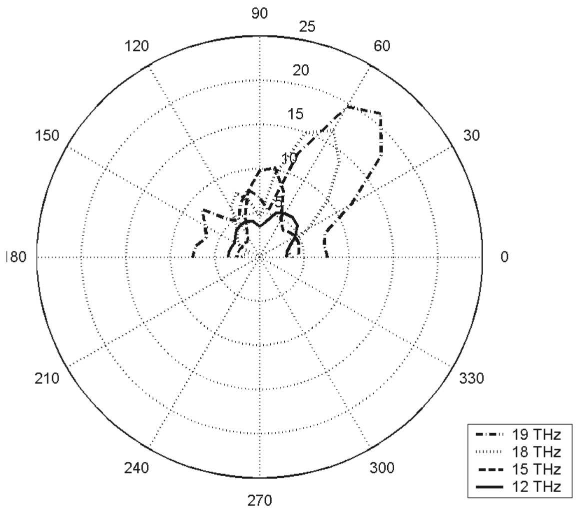

Fig. 20. Radiation pattern for the total electric field at φ=0˚ for Case 2.

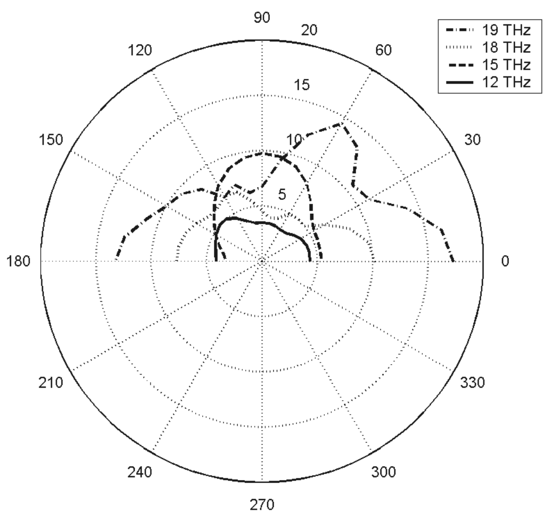

Fig. 21. Radiation pattern for the total electric field at φ=90˚ for Case 2.

Recursively increasing the number of loops should enhance all of these factors, i.e. narrow the directionality and strengthen the intensity. Further, taken in conjunction with the other patterns, e.g. those at 18 and 19 THz, one can argue that a variable frequency source is possible using the same circuit but a narrowband source.

Considering the (3-D) radiation patterns for both the half-circle (Fig. 17) and two half-circles called Case 2 (Fig. 22), reinforces the conclusion that both the directivities and intensities of the two-loop case are much better. This is very noticeable for the higher frequencies, where Fig. 17 shows a very distorted radiation pattern around f = 18 THz, while Fig. 22 shows fewer side lobes along with a main lobe that has a high-peak value that is directed at ~30-35º from the circuit normal (θ=90˚). Further, at f = 8 THz, not shown in Figs. 20 and 21 for Case 2, the radiation pattern is more dipole-like compared to the half-circle case and this is expected to be mirror symmetric about the XY plane.

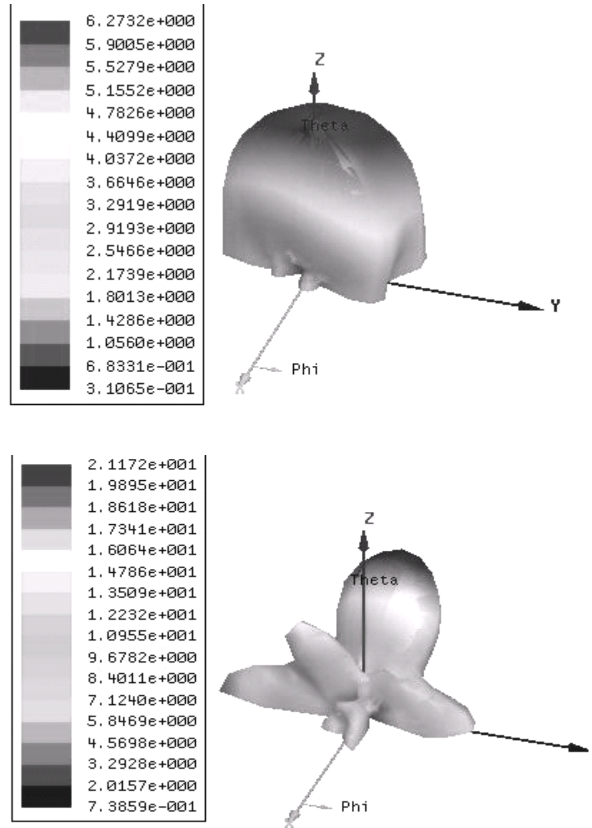

Fig. 22. 3-D Radiation patterns (mV) for the two, half-circles: Case 2 at 8 and 19 THz.

Another figure-of-merit, related to the efficiency of Eq. 6, that can be defined and that is useful to characterize a radiating structure, is the radiation coupling impedance:

$$Z_{rc} = \frac{|E_{peak}\lambda|^2}{P_{total}} \quad (\Omega) \qquad (10)$$

where this is also a useful measure for a laser driven accelerator. Here it is a measure of how much power is converted into radiation. Thus, for our cases and for electro-optic acceleration, we want to maximize it but for many other devices such as inductors, the goal reverses. Table I emphasizes that radiation coming out of the two half circles can be both higher and lower than for one half-circle based on interference effects and gives a rather different picture than

TABLE I
COMPARISON OF COUPLING IMPEDANCE FOR DIFFERENT CASES

Frequency (THz)	Z_{rc} (Ω) (*One Half-Circle*) Fig. 13 when $T = 0$	Z_{rc} (Ω) (*Two Half-circles*) Fig. 18 when $d = 0$
2	0.16	0.20
4	1.76	2.46
8	19.53	38.81
12	74.82	33.64
15	87.79	105.06
18	89.6	273.90

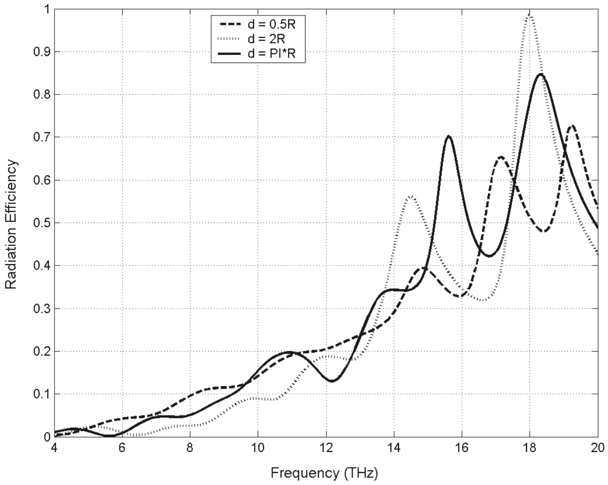

Fig. 23. Radiation efficiency curves for different values of the separation distance *d*.

the total radiated power. In the next section, a new structure will be analyzed to exploit the fact that a change of frequency can achieve constructive or destructive interference.

C. Two-Loop, One-Period N=1 With Different Separation Distances

Fig. 18 shows a top-view of the simulated structure. The main idea is to achieve a constructive radiation of the two-half circles, using *d* as a tuning element to obtain higher radiated power or radiation efficiency as well as directivity. In order to do this, a transmission line of distance *d* or some functional equivalent such as multi-port feeds is inserted between the two half-circles. By changing the distance *d*, the phase difference of the EM-waves propagating along the two half circles is controlled to provide the desired effect. It is important to mention that the radiated power will be a function of only the frequency *f* and the distance *d* when keeping all the other parameters, e.g. the shape, fixed. Further, the distance *d* affects both the amount of radiated power and the frequency at which the maximum values of radiation occur.

FDTD simulation results are shown in Fig. 23, where we observe that the cases for *d*=0.5R and πR correspond most closely to Case 2 of Fig. 19, except for frequency shifts, and the same analysis leads to similar conclusions here as well, although the quadratic variation with frequency is more obvious in Fig. 23.

Although the *d*=πR resonance near 16 THz has high efficiency and narrow bandwidth, the peak-to-valley ratio, efficiency, and width of the *d*=2R resonance at 18 THz is more remarkable. In this case, the circles are the tuning elements for the 90º turns spaced at 2R. These and other options are being studied further to determine what to optimize (and how) based on their differing potential applications.

VII. Another Figure-of-Merit for Applications

For completeness, we include another F-o-M that is especially relevant for sources (and detectors) called the brightness. Control of the 6-dimensional phase space of a particle or photon beam begins with production and proceeds through every subsequent step until extraction and use. A quantity that best represents the fully invariant 6-D phase space for linear, time independent systems is the normalized brightness:

$$B_n^6 = \frac{\mathrm{N}_\gamma}{\varepsilon_{\mathrm{nx}}\varepsilon_{\mathrm{ny}}\sigma_t\sigma_\omega} \qquad (11)$$

where N_γ is the number of quasi-particles (electrons or photons) in a bunch, ε_{nx} and ε_{ny} are the transverse, normalized emittances and σ_t and σ_ω are the corresponding longitudinal parameters - the bunch's rms length and energy spread. For photons, one can simplify Eq. (11) to a photon density:

$$B_n^6 = (4\pi)^2 \frac{\mathrm{N}_\gamma}{\lambda^2\sigma_t\sigma_\omega/\varpi}\eta \le 7\cdot 10^{16}\eta/\lambda^3. \qquad (12)$$

Even for an effective efficiency η«1, bound implementations are far preferable since this is a bright source by virtually any standard. Further, we define an intense source as one where N_γ/λ^3 »1. We should also note that brightness is not an inherent characteristic of any beam but of its original production source, focus and containment environment.

VIII. Conclusions And Future Research

A variety of configurations were studied in terms of their basic shape parameters, which were then related to their respective resonance patterns. Figures-of-merit were defined and calculated for the various structures, which showed that several of them were quite interesting. Further, we could understand the basic characteristics of the efficiency diagrams and radiation patterns in terms of a sum of simplified dipole radiators, e.g. the low frequency variation in the radiated power and its angular distribution as well as the number of lobes and their distributions at higher frequencies. Various interference effects were studied in terms of both structural shape and tuning parameters to improve output intensity, bandwidth and directionality.

We did not discuss any options on how we could realize such devices [1] here because our main goal was to concentrate on the radiative characteristics and determine whether the underlying electromagnetics we were assuming was sound. Clearly, there are some very important questions to be pursued on the physical device side - some of which are quite fundamental. On the production side, depending on the option, the challenges don't lie in the feature sizes but in the materials and operating conditions such as the excitation or drive source [8]-[9], ballistic transport conditions [10] and replenishing the pulse current and voltage as the radiation process proceeds at high efficiency. Nevertheless, the results are very promising, e.g. the *d*=2R case in Fig. 23 does not rely on long distance ballistic transport around the loops to be effective.

We did not address possibilities for coherent effects for bound electrons [1] even though we believe that these may be possible in such structures because, as we defined them in Section II, they can not be calculated with present codes. However, one expects some degree of coherence or cooperative effects to be observable whenever $\lambda \gg \sigma_e$, the rms longitudinal, electron bunch length. In Ref. [1], we mentioned some possibilities related to the Smith-Purcell effect. Looking at Figs. 20-22, one sees an intense lobe at ~50º to the circuit plane, extending along the –X direction along the beam direction that seems ideal for a variety of either bound or free electron and single or double plane combinations.

Currently available codes, while very useful, don't have the capabilities that are required here because they were not developed for such applications. Beyond coherence effects, examples include pulsed circuits, nonlinear and parametric frequency effects. Still, the frequency domain code HFSS allowed us to demonstrate the potential of this approach. Thus, we still have found no impediments to pursuing it. Further, during the course of this work, we have developed some ideas on how to actually optimize the circuit design for such structures in terms of the radiation coupling impedance Z_{rc}, the efficiency η or the brightness *B* depending on the application.

In this, we can take advantage of some of the analytic possibilities that were developed and used here [11]. The reader is referred to Ref. [1] for a broader discussion of the possibilities and additional references. As noted there, even the differing uses of metals in such devices, as opposed to semiconductors, is too broad to discuss here as are the differences between metals such as Al and Au [12] for use in fast THz laser drive systems. Further, as noted above, we need better models for materials such as the damage and dielectric constants as a function of the frequency ω or pulse length τ.

Acknowledgments

This work was supported by the US Department of Energy under contract *DE-ACO3-76SF00515.* The authors would also like to thank Patrick King and Jeff Schuetz of Ansoft Corporation for providing the HFSS code and also for their technical support.

References

[1] Y. A. Hussein and J. E. Spencer, "Novel possibilities for coherent radiation sources," in *2004 IEEE MTT-S Int. Sym. Dig*., to be published.

[2] P. H. Siegel, "Terahertz technology," *IEEE Trans. Microwave Theory Tech*., vol. 50, No. 3, pp. 910-928, Mar. 2002.

[3] S. J. Allen, "Terahertz dynamics in semiconductor quantum structures,"*27th Int'l. Conf. Infrared and Millimeter Waves*, Sept. 2002.

[4] W. Ha, J. Mansell, T. Plettner, J. Wisdom, J. E. Spencer "Miniaturization techniques for accelerators," *2003 Particle Accelerator Conf*., pp. 1861-1864, May 2003. Available: http://www.slac.stanford.edu/pubs. #SLAC-PUB-9882.

[5] D. M. Sheen, S. M. Ali, M. D. Abouzahra, and J. A. Kong, "Application of the three-dimensional finite-difference time-domain method to the analysis of planar microstrip circuits," *IEEE Trans. Microwave Theory Tech.,* vol. 38, pp.849-857, July 1990.

[6] A. Taflove, *Computational Electrodynamics: The Finite-Difference Time-Domain Method.* Norwood, MA: Artech House, 1995.

[7] Ansoft Corporation high frequency structure simulator (HFSS), version 9.0 for Windows, released May 2003.

[8] Power sources are currently available commercially that could provide higher gradients than RF under this scenario at 50 MHz rep rates e.g. see the IMRA America, Inc. website. Research lasers have been demonstrated above 30 GHz and it appears that beat-wave lasers based on differing dopants of YAG should be able to provide THz.

[9] C. B. Schaffer, A. Brodeur , and E. Mazur, "Laser-induced breakdown and damage in bulk transparent materials induced by tightly focused femtosecond laser pulses," *Measurement, Science and Technology Meas* , vol. 12, pp. 1784-1790.

[10] Z. S. Gribnikov, N. Z. Vagidov, V.V. Mitin, G. I. Haddad, "Theory of unipolar ballistic and quasiballistic transit-time oscillators for a terahertz range," *Physica.E.*, pp. 89-94, Jan. 2003.

[11] Y. A. Hussein, J. E. Spencer, S. M. El-Ghazaly, "On the design and optimization of coplanar waveguides using evolutionary approaches," in *2004 IEEE AP-S Int. Sym. Dig*., to be published.

[12] C. Guo, G. Rodriguez, A. Lobad, and A. J. Taylor," Structural phase transition of aluminum induced by electronic excitation," *Phys. Rev. Lett* 84, pp. 4493-4496, May 2000.